ACS OMEGA

Open Access

This article is licensed under CC-BY-NC-ND 4.0

http://pubs.acs.org/journal/acsodf

Article

Making Healthcare Accessible: A Rapid Clean-Room-Free Fabrication Strategy for Microfluidics-Driven Biosensors Based on Coupling Stereolithography and Hot Embossing

Haoliang Lu, Almas Rakhymzhanov, Ulrich Buttner, and Dana Alsulaiman*

Cite This: ACS Omega 2024, 9, 38096−38106

Read Online

ACCESS | Metrics & More | Article Recommendations | Supporting Information

ABSTRACT: Microfluidics offers transformative potential in healthcare by enabling miniaturized, user-friendly, and cost-effective devices for disease diagnostics among other biomedical applications; however, their meaningful adoption is severely hindered, especially in developing countries and resource-limited settings, by the cost, time, and complexity of their fabrication. To overcome this barrier of access, this work develops a novel approach for highly efficient (<4 h), cost-effective, and clean-room-free fabrication of functional polydimethylsiloxane (PDMS)-based microfluidic devices based on coupling stereolithography three-dimensional (3D) printing with hot embossing. The strategy exhibits high fidelity between the digital design and final device, remarkable transfer accuracy between the 3D print and poly(methyl methacrylate) (PMMA) mold, in addition to highly smooth surfaces (R_a < 1 μm). To establish the versatility of the approach and performance quality of the fabricated devices, three advanced microfluidics-driven biosensing platforms are developed: a microsphere droplet generator, a stop-flow lithography-based hydrogel microparticle synthesizer, and a hydrogel postembedded microfluidic device for multiplexed biomarker detection. As a proof-of-concept, the latter platform was applied to the multiplexed detection of microRNA, a highly promising class of liquid biopsy biomarkers for many diseases including cancer. Notably, the ability to demonstrate multiplexed sensing of disease biomarkers within devices made through a facile, rapid, and clean-room-free strategy demonstrates the immense potential of this fabrication approach to accelerate the adoption and advancement of biomedical microfluidic devices in practice and in resource-limited settings.

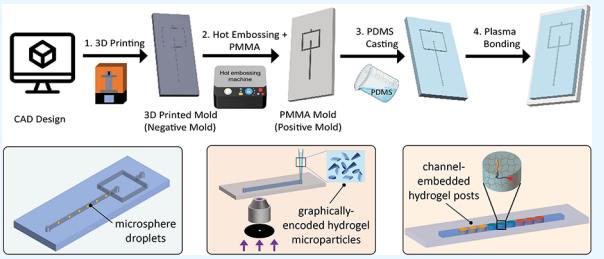

INTRODUCTION

Given the characteristics of low sample and reagent consumption,[1] laminar flow profiles,[2] and fast reaction kinetics,[3] the field of microfluidics offers immense potential to revolutionize the healthcare sector by offering portable and easy-to-handle platforms including organ-on-a-chip devices,[4] wearable sensors,[5] and lab-on-a-chip devices for drug screening,[6] tissue engineering,[7] and point-of-care biosensing.[8−13] Despite these promises, the widespread and meaningful adoption of microfluidic systems remains elusive, especially in resource-limited settings where there is a pressing and urgent need for infectious disease detection and early screening tools. A major barrier lies in the high cost and complexity of traditional microfluidic device-prototyping approaches which are unrealizable in low-resource settings. These conventional fabrication methods involve laborious processes such as master mold preparation using epoxy resin SU-8 and subsequent replication, necessitating access to cleanroom facilities, specialized equipment, and skilled personnel.[14]

Although three-dimensional (3D) printing has emerged as an attractive and inexpensive alternative for microfluidic device fabrication,[15] challenges persist regarding limited resolution and material compatibility (see Supporting Information, Table S1).[16] Stereolithography (SLA), a promising 3D printing method, uses layer-by-layer photopolymerization of a photoresin precursor to achieve high-resolution 3D structures in the order of 25 μm.[17,18] However, challenges with high surface roughness (R_a)[19] and SLA resin compatibility with polydimethylsiloxane (PDMS) - which is the most widely used thermoset polymer in microfluidics - severely limit its use in mold preparation. For example, incomplete PDMS polymerization occurs using conventional resin molds due to the presence of unreacted monomers on the surface of the 3D print.[20] Furthermore, while hot embossing is a high throughput and low-cost technique, it conventionally requires the use of silicon or metal molds,[21] expensive equipment, and complicated postprocessing steps.[22,23]

Herein, by coupling SLA with hot embossing, a cost-effective, user-friendly, and time-efficient method for micro-

Received: June 3, 2024
Revised: August 1, 2024
Accepted: August 16, 2024
Published: August 23, 2024

© 2024 The Authors. Published by American Chemical Society

Scheme 1. Schematics of the PDMS Microfluidic Device Fabrication Strategy and Three Types of Microfluidics-Driven Biosensor Devices[a]

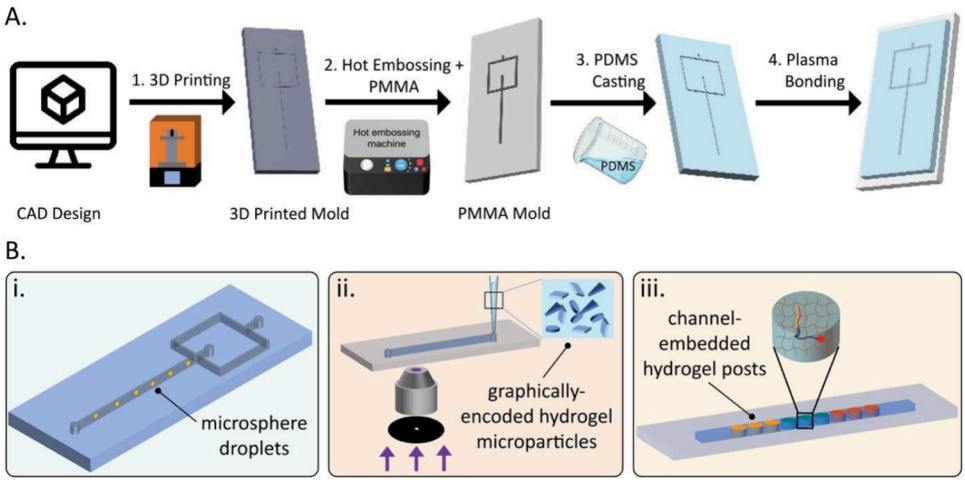

[a]A. Schematic of the PDMS microfluidic device fabrication strategy based on SLA 3D printing coupled with hot embossing where (1) a 3D print of the desired design is used to create (2) a PMMA mold via hot embossing. This PMMA replica serves as a mold to (3) cast PDMS and fabricate the working device, commonly after (4) plasma bonding onto a glass slide. B. Schematic representation of the three types of microfluidics-driven biosensor devices fabricated with the proposed approach: i. a microsphere droplet generator, ii. an SFL-based hydrogel synthesizer, and iii. a hydrogel post-embedded device for multiplexed biomarker detection.

fluidic chip fabrication is developed, which produces robust and functional devices with high resolution, high repeatability, and low R_a (<1 μm) without the need for a cleanroom facility or the use of metal or silicon molds (Scheme 1). Importantly, by introducing the hot embossing process, we avoid the compatibility issues between conventional SLA resins and PDMS; the double casting technique produces a much more compatible polymer template, specifically PMMA, for PDMS casting. Table S2 in the Supporting Information illustrates the competitiveness and performance of our approach compared to conventional strategies in terms of cost-effectiveness, time efficiency, resolution, advantages and limitations. Using the proposed approach, a computer-aided design (CAD) can be transformed into a working microfluidic device in less than 4 h. A schematic diagram illustrating the entire fabrication workflow and the duration of each step can be found in the SI (Figure S1). Briefly, a CAD design is 3D printed into a mold which is then sandwiched between a poly(methyl methacrylate) (PMMA) chip and a piece of quartz to enable hot embossing into a PMMA replica. This PMMA replica then serves as a mold for the desired PDMS-based microfluidic device, commonly assembled via plasma bonding to a cover slide or coverslip (Scheme 1A). To demonstrate the versatility and functionality of this approach, three microfluidic devices of relevance to biosensing applications are developed: a microsphere droplet generator, a stop-flow lithography (SFL)−based hydrogel microparticle synthesizer, and a hydrogel postembedded microfluidic device for multiplexed microRNA biomarker detection (Scheme 1B). The proposed facile yet highly accessible approach broadens the scope and potential of microfluidic devices in practice by eliminating the need for trained personnel or expensive equipment and setups, thereby pushing the frontiers of microfluidics-driven biomedical devices into resource-limited environments, where they are needed the most.

RESULTS AND DISCUSSION

Design, Fabrication, and Characterization of the 3D Prints. As a first demonstration, we sought to develop a hydrodynamic flow-focusing device, comprising a narrow nozzle channel designed to promote the squeezing effect of the central flow and a wider main channel with widths of 154 and 300 μm respectively, and a channel depth of 126 μm as detailed in Figure 1A. After the device was designed on SOLIDWORKS, preparing the 3D prints involved using an SLA 3D printer in which UV light photochemically solidifies the printer resin, forming one layer of the predesigned 3D object.[24] A commercial resin (TR300 Ultra-High Temp 3D Printing Resin, Phrozen Technology, Taiwan) with ultrahigh temperature resistance was specifically chosen in this work to ensure compatibility with subsequent hot embossing steps. The duration of UV exposure for each layer can considerably affect the quality of the printed surface and channels, particularly when the designed channels are in microscale dimensions.[25,26] The exposure time was therefore optimized to ensure high accuracy and reproducibility of the 3D prints. Figure 1B shows brightfield microscopy images of the main and nozzle channels prepared under different exposure times. For the main channel, with profiles plotted in Figure 1C (i), 3 s of exposure time (dark blue line) resulted in the lowest accuracy, with dimensions (width = 221 μm and depth = 116 μm) lower than the design specifications (dashed line). After complete solidification of the resin, excessive UV light exposure can result in light scattering and subsequent curing of the adjacent unexposed resin, causing the solid structure to expand and thereby producing channels with smaller dimensions than the design specifications. Reducing the exposure time to 1 s per layer (yellow line) also resulted in low accuracy with larger channel dimensions (308-μm wide and 128-μm deep) than the design specifications. In this case, contrary to overexposure, insufficient UV light energy to cure the photoresin caused delamination in the structure due to poor layer adhesion. The highest accuracy in channel

https://doi.org/10.1021/acsomega.4c05196
ACS Omega 2024, 9, 38096−38106

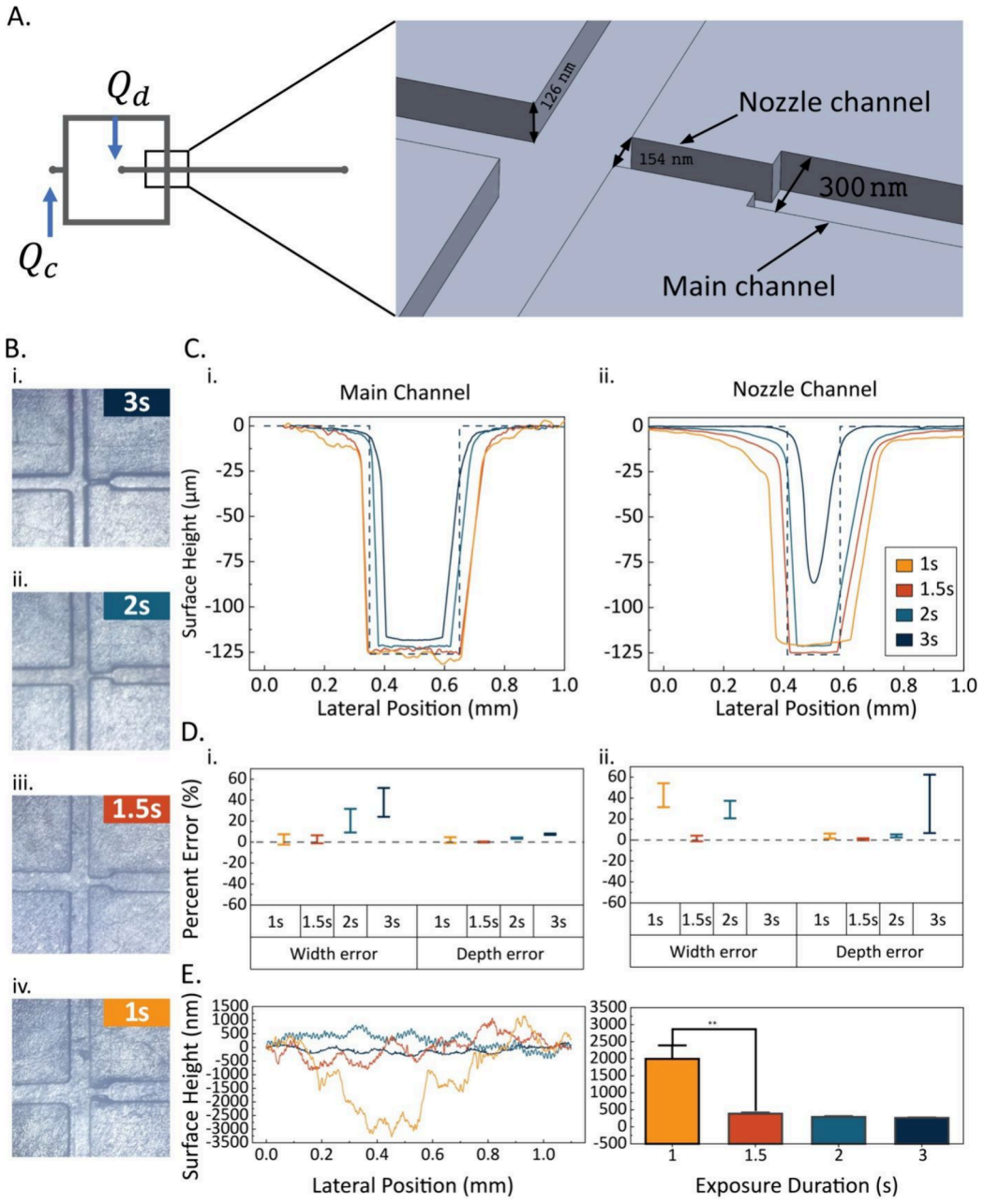

Figure 1. A. CAD design of the flow-focusing device with a magnified view of the main channel and nozzle channel highlighting the design dimensions. B. Bright-field microscopy images of the channel junction made from 3D printing under (i) 3 s, (ii) 2 s, (iii) 1.5 s, and (iv) 1 s of exposure time per layer. C. Stylus profilometer profiles of the (i) main channel and (ii) nozzle channel printed under different exposure times compared to the design (dashed line). D. Percentage error of the (i) main channel and (ii) nozzle channel compared to the design under different exposure times. E. Surface roughness of the 3D prints, plotted as surface height versus lateral position (left) or against exposure time (right). ** indicates a statistically significant difference (p-value = 0.0082, unpaired t test).

dimensions and the lowest percentage error between the design and print was achieved using an exposure time of 1.5 s (Figure 1D), which produced channels with a width of 302 μm and depth of 126 μm.

For the nozzle channel, with profiles plotted in Figure 1C (ii), we observed that the exposure duration of 1.5 s per layer also achieved optimal results. This condition achieved the greatest agreement between the design and the resulting channel dimensions, with the lowest percentage error as depicted in Figure 1D (ii). Furthermore, the R_a of the devices was also characterized and plotted in Figure 1E. The results show a negative correlation between exposure time and R_a value, wherein increasing the exposure time resulted in lower R_a value and a smoother channel. Considering these results, the 1.5 s exposure time per layer was deemed as optimal to ensure the highest accuracy in channel dimensions and surface quality.

Development and Characterization of the PMMA Replicas. To develop the PMMA replicas from the 3D prints, hot embossing was used by sandwiching the 3D print between a PMMA chip and a piece of quartz and placing this assembly into a hot embossing instrument. The plate inside the hot embossing instrument was heated above the glass transition temperature of PMMA to enable the PMMA to reach a

https://doi.org/10.1021/acsomega.4c05196
ACS Omega 2024, 9, 38096−38106

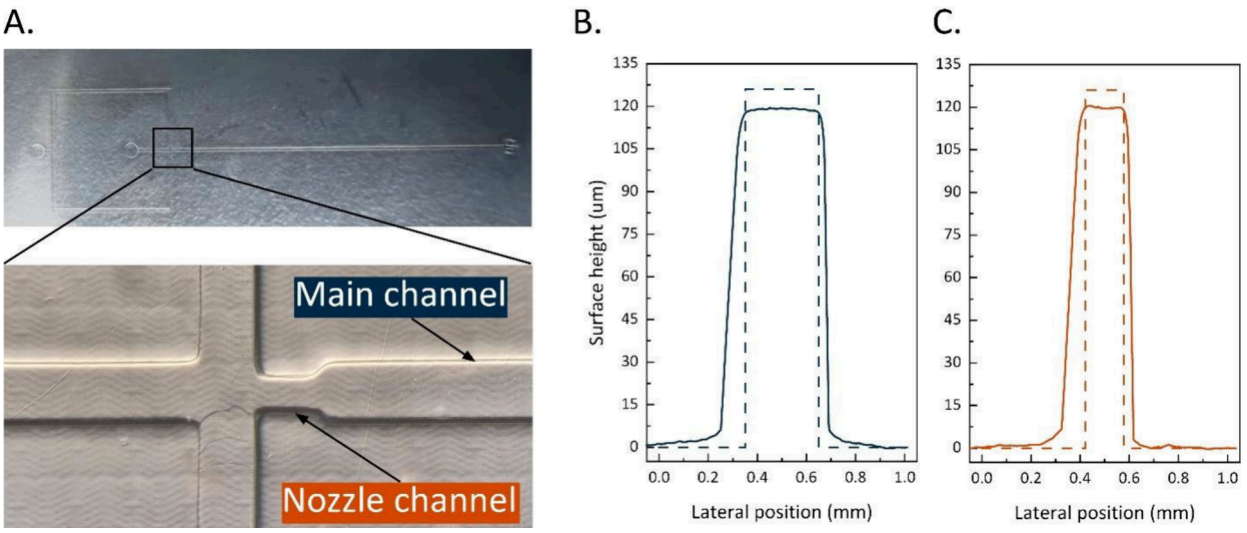

Figure 2. A. Overview and zoom-in view of the microfluidic channel on the PMMA replica, showing well-defined channel walls and high feature integrity. Profiles of the main channel (B) and nozzle channel (C) on the PMMA replica compared to the design (dashed line), showing high replication quality.

Table 1. Comparison between the Design Dimensions versus the 3D Prints, Replicated PMMA, and the Final PDMS Device Channel Dimensions

Channel type	Design height (μm)	Printed height (μm)	Mean replicated height (μm)	Mean height in PDMS (μm)	Design width (μm)	Printed width (μm)	Mean replicated width (μm)	Mean width in PDMS (μm)
Main channel	126	126 ± 0.2	119 ± 1	119 ± 1	300	302 ± 2	301 ± 3	302 ± 1
Nozzle channel	126	125 ± 1	120 ± 1	120 ± 1	154	153 ± 1	155 ± 1	156 ± 1

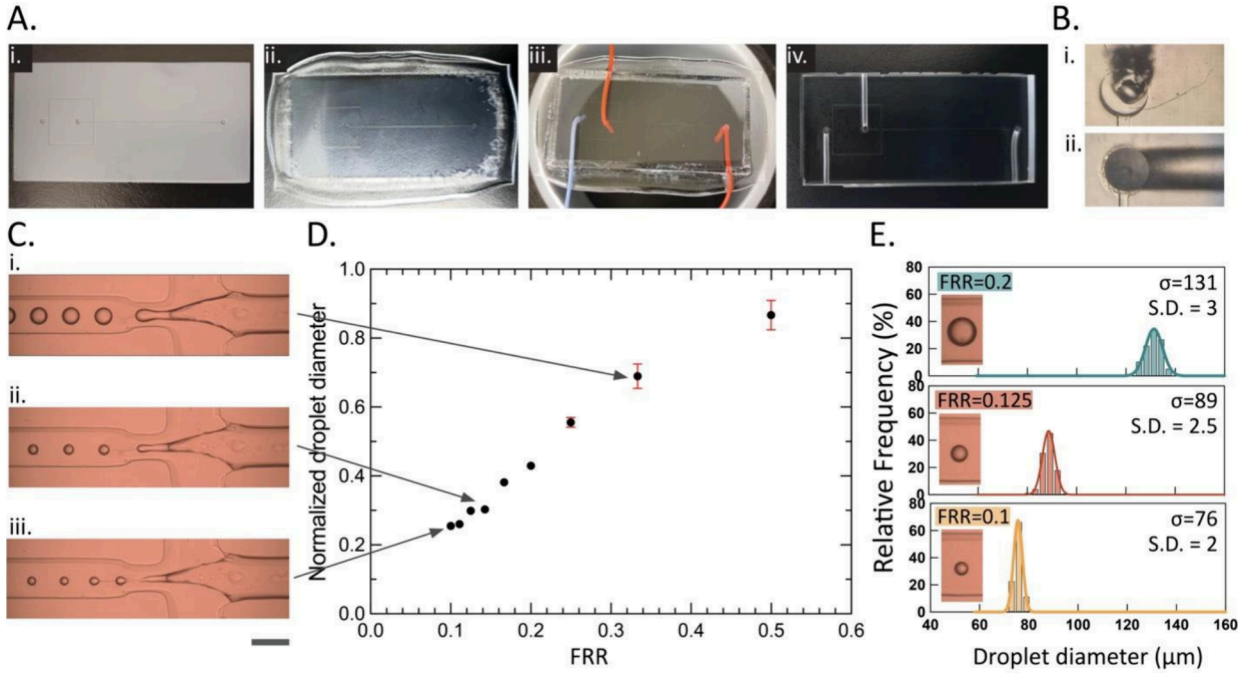

Figure 3. Fabrication and performance of the flow-focusing droplet generator device. A. Steps describing the preparation of the PDMS device, showing i. the 3D-printed mold for hot embossing, ii. the PMMA mold after hot embossing, iii. the PDMS cast on the PMMA mold with tubes inserted at the inlet and outlet, and iv. the final PDMS microfluidic device. B. Magnified view of i. an inlet hole created using a manual punch and ii. an inlet hole and lateral channel created using the plastic tube method developed in this work. C. Photos of monodisperse microsphere droplets generated by the fabricated device using three different flow rate ratios (scale bar shows 300 μm). D. Normalized droplet diameter ((droplet diameter)/(channel width)) versus FRR showing an increase in droplet diameter with increasing FRR. E. Histograms of droplet diameter at varying FRR, with Gaussian fittings showing a low standard deviation (S.D.) indicative of the generation of highly reproducible and monodisperse droplets.

https://doi.org/10.1021/acsomega.4c05196
ACS Omega 2024, 9, 38096−38106

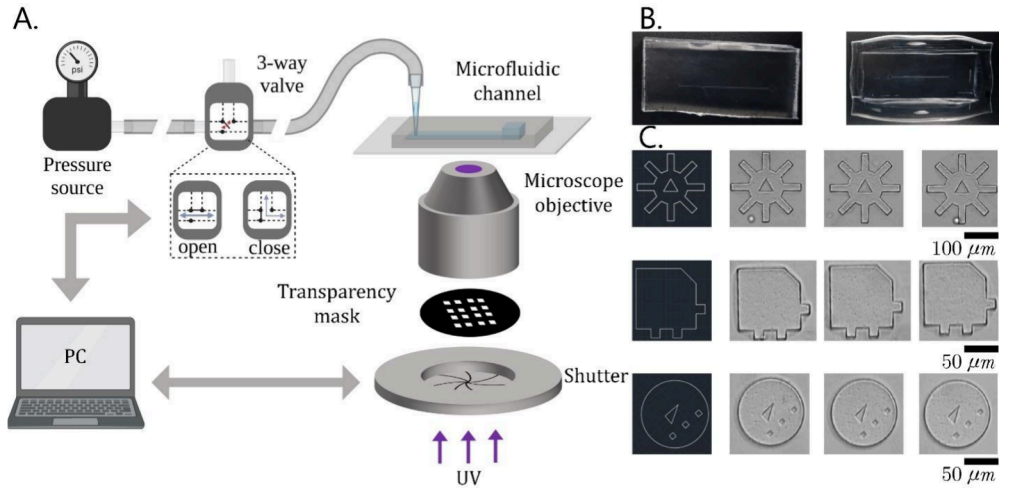

Figure 4. A. Schematic showing the experimental setup and process of SFL. B. Photo of the SFL-based microparticle synthesizer PDMS device (left) and its PMMA mold (right) C. Photomasks with well-defined graphical codes (left) and images of three representative graphically encoded microparticles (right) fabricated within the SFL microfluidic device.

rubbery state,[27] and a pressure of 400 MPa was applied to the assembly as the temperature increased to 165°C. These parameters were chosen to allow PMMA to fully conform to the mold features and achieve accurate depth and width replication. The heating duration was set to 10 min, whereas the cooling duration was optimized to 1 h. Herein, the surface finish and channel dimensions of the PMMA molds were characterized to investigate the R_a and replication accuracy. Figure 2A shows photographs of the microfluidic channel with a magnified view of the nozzle region. Using a stylus profilometer, profiles of the main and nozzle channels were measured as shown in Figure 2B,C, respectively, with solid lines indicating measured values and dashed lines indicating the design dimensions. The hot-embossed main channel (solid blue line) exhibited a width of 300.2 μm and a depth of 119.4 μm, whereas the nozzle (solid red line) exhibited a width of 151.8 μm and depth of 120.4 μm. This corresponds to a remarkable PMMA replication accuracy of over 98% in width and 94% in depth compared to the design dimensions.

Next, to investigate the reproducibility and validate the accuracy of the printing and hot embossing steps, three additional PMMA replicas were produced from three distinct 3D prints following the same hot embossing protocol. Table 1 shows a comparison between the design dimensions versus the printed and replicated channel dimensions as well as the dimensions of the final PDMS device. In addition to the high reproducibility demonstrated by the low standard deviation in the dimensions recorded, the results show two additional findings: i. the hot embossing process rather than the printing process contributes most significantly to the discrepancy between the design and the PMMA replica, and ii. the process introduces errors mainly to the vertical (rather than the lateral) dimension of the device. Specifically, the data reveal that for a 6% discrepancy in the vertical dimension, less than 1% arises from the 3D printing process while 5% arises from the hot embossing process, likely due to inadequate pressure. In the case of the lateral channel dimensions, a minor less (than 1%) error was observed in the PMMA replicas compared to the design. Consequently, the overall replication quality exceeds 94% and 99% in the vertical and lateral dimensions, respectively, while maintaining low surface roughness, with an R_a value of 381 ± 29 nm. Achieving a smooth surface ensures better wettability, bonding quality, while minimizing turbulence and absorbance of contaminants.[28,29]

Preparation and Assembly of the Microfluidic Device. Finally, using the PMMA replica as a mold, we prepared a PDMS-based droplet generator microfluidic device with smooth interfacial holes and lateral channels, following the procedure shown in Figure 3A. Briefly, tubes were inserted from the sides of the microfluidic structure and aligned using a simple PMMA frame with drilled holes, to create interfacial connections from the peripheral equipment to the device (Supporting Information, Figure S2). After casting PDMS onto the PMMA mold, successful cross-linking occurred with an excellent surface finish and no evidence of any residual uncured PDMS on the surface of the mold. For comparison, the standard method of manual punching was used to create an interfacial hole, as shown in Figure 3B (i). The hole appeared rough and crooked and contained some residual PDMS chunks, all of which may cause clogging of the microfluidic channels and leakage. In contrast, Figure 3B (ii) shows an interfacial hole created using the described protocol, which appeared smooth, straight, and more durable compared to that created using the standard method of manual punching.

Finally, the microfluidic device was assembled by bonding the PDMS onto a glass slide to enclose the microfluidic channels after a 40s plasma treatment was implemented to remove contaminants and impurities on the surfaces while introducing reactive chemical groups to improve surface adhesiveness and bonding.[30,31] The total duration of the microfluidic device fabrication strategy from design to device was less than 4 h.

Demonstrating Device Functionality via Three Microfluidics-Driven Biosensing Platforms. Most microfluidic devices are purchased commercially or fabricated in cleanroom facilities following multiple tedious and expensive steps.[32−34] To demonstrate the feasibility and functionality of the devices prepared using our strategy, we first developed a microsphere droplet generator, which is a versatile device that can be used to produce highly uniform aqueous droplets for advanced biosensing applications such as ddPCR.[35−38] Following the proposed fabrication approach, the assembled device was connected to liquid sources (Figure 1A), with the central and side channels dedicated to the aqueous and organic phases,

https://doi.org/10.1021/acsomega.4c05196
ACS Omega 2024, 9, 38096−38106

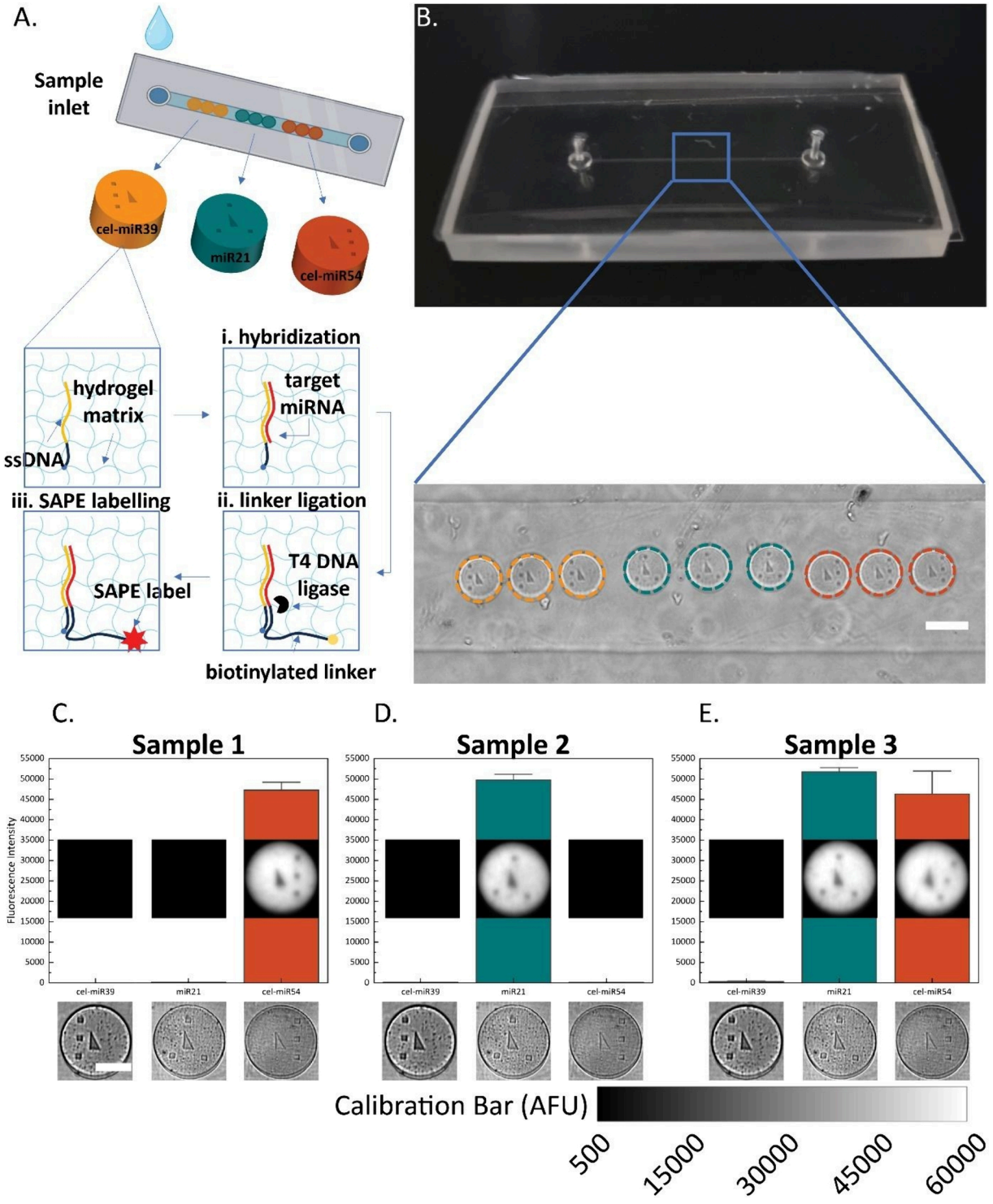

Figure 5. Schematic diagram of the hydrogel postembedded microfluidic device for multiplexed detection of three microRNA targets, showing the three-step miRNA sensing assay occurring within the posts: i. hybridization of the target to the ssDNA probe, ii. ligation of a biotinylated linker using T4 DNA ligase, and iii. labeling of SAPE dye. B. Photograph of the fabricated microfluidic device with a magnified brightfield microscopy image of the graphically encoded hydrogel posts embedded within the microfluidic channel (scale bar shows 100 μm). Fluorescence intensity of the hydrogel posts after the detection of miRNA levels from (C) sample 1 containing 100 nM of *cel*-miR-54 (scale bar shows 50 μm), (D) sample 2 containing 100 nM of *hsa*-miR-21, and (E) sample 3 containing 100 nM of *hsa*-miR-21 and 100 nM of *cel*-miR-39.

respectively. The volumetric flow rate of the aqueous dispersed phase (Q_d) was kept constant at 5 μL/min, while the volumetric flow rate of the organic continuous phase (Q_c) was gradually increased. The flow of droplets generated under varying flow rate ratios ($FRR = \frac{Q_d}{Q_c}$) was observed under a microscope and recorded by a high-speed camera. Figure 3C shows screenshots of the videos recording monodisperse microsphere droplets of varying diameters generated by the fabricated device under varying flow rate ratios. The normalized droplet diameter ((droplet diameter)/(channel

https://doi.org/10.1021/acsomega.4c05196
ACS Omega 2024, 9, 38096−38106

width)) is plotted against FRR in Figure 3D, showing the increase in droplet diameter with increasing FRR. Histograms of the droplet size distribution under various FRR conditions are plotted in Figure 3E, with Gaussian fittings showing high reproducibility in droplet sizes and a low standard deviation. These results demonstrate the potential of the proposed fabrication approach to overcome the limitations of traditional fabrication methods and its feasibility in the preparation of high-quality droplet generation devices, pertinent to many biomedical and biosensing applications including ddPCR.

Despite its promise, ddPCR offers limited multiplexing capabilities, often enabling the detection of only a single biomarker target at a time. Advanced healthcare and diagnostic applications necessitate multiplexed biosensing systems that enable the detection of multiple disease biomarkers simultaneously. To this end, the proposed fabrication approach was used to prepare a microfluidic device enabling multiplexed biosensing based SFL-enabled hydrogel microparticle synthesis. First reported by Denkukuri et al.,[39] SFL is a microfluidics-driven approach for high-throughput fabrication of graphically encoded hydrogel microparticles within microfluidic channels filled with a UV-cross-linkable hydrogel precursor solution.[40] Figure 4A illustrates the configuration of an SFL system, where UV light passes through a defined photomask that is placed in the field-stop of an inverted fluorescence microscope. When the fluid flow within the microfluidic channel stops and upon exposure to UV light, the hydrogel precursor solution is cross-linked via photoinitiated UV polymerization into high-resolution graphically encoded hydrogel microparticles as outlined by the photomask defining a specific micropattern (of varying shapes or graphical codes). The following three steps of i. stopping the fluid flow, ii. polymerizing the particles, and iii. flowing the fluid, are cycled until the desired number of particles are fabricated.

To our knowledge, all prior demonstrations of microfluidic devices for SFL have been based on traditional fabrication approaches; thus, we investigated herein the feasibility of using our clean-room-free approach to prepare these devices with greater time efficiency and cost-effectiveness. Figure 4B shows the microfluidic device fabricated by the proposed strategy which contains a 300 μm wide and 40 μm tall straight channel with a pair of holes on each side as the inlet and outlet. The device was assembled by placing the PDMS chip onto a glass coverslip which was coated with a thin layer of PDMS, which serves to seal the device while acting as an oxygen inhibition layer to prevent the hydrogel particles from sticking to the channel surface. To assess the functionality of the microfluidic device for SFL-based particle synthesis, a hydrogel precursor solution based on a mixture of polyethylene glycol diacrylate, polyethylene glycol, and photoinitiator was prepared and inserted into the inlet of the device, which was connected to a pressure source controlled by a microprocessor.[41] After running the SFL procedure within the device, we collected the synthesized particles from the outlet channel and obtained brightfield microscopy images of the particles (under a 20x objective lens). The images showed high-resolution particles with well-defined shapes, including 100 μm diameter circular particles with 6 μm square motifs (Figure 4C). The presented results further demonstrate the versatility of the fabrication strategy and the feasibility of using the prepared devices in SFL-based microparticle synthesis applications, including the development of graphically encoded hydrogel particles for multiplexed biosensing applications.

As a third application of the proposed fabrication approach, we developed a microfluidic device with embedded and graphically encoded hydrogel posts designed for multiplexed detection of clinically relevant disease biomarkers (Figure 5A). As a proof-of-concept, the device was applied to the multiplexed detection of microRNA (miRNA), which are short (~19−25 nt) noncoding RNA that hold promising potential as liquid biopsy biomarkers for many diseases including cancer.[42] The same channel design as the SFL device was used in this application; however, to enable immobilization of the hydrogel posts to the channel walls, the device was assembled by directly placing the fabricated PDMS chip onto a clean coverslip (without coating with a PDMS layer) (Figure 5B). To prepare the hydrogel posts for biosensing applications, the aforementioned hydrogel precursor was prepared with a 10 μM concentration of a desired bioreceptor, and this solution was infused into the microfluidic device. To enable covalent functionalization into the hydrogel matrix, the probe used herein comprised an acrydite-modified ssDNA strand designed with a sensing region complementary to the target miRNA and a common region complementary to a universal biotinylated linker. Similar to the SFL strategy, graphically encoded hydrogel posts were then synthesized inside the channel via photoinitiated UV polymerization through defined photomasks, each with a specific graphical code corresponding to a different target biomarker (Figure 5A). Three posts were prepared for each code to facilitate statistical analysis of the results. In this instance, the platform was designed to detect three different miRNAs: *cel*-miR39, *cel*-miR-54, and *hsa*-miR-21. The latter miRNA, *hsa*-miR-21, is a well-established oncogenic miRNA that is upregulated in many cancer types.[43]

After fabrication of the hydrogel postembedded microfluidic device, we sought to investigate its ability to detect miRNA expression levels in a multiplexed manner. Dysregulation in the levels of certain miRNA panels can be used to provide highly accurate clinicopathological information about a disease such as cancer diagnosis. To this end, we prepared three model biological samples, with varying expression levels of the three miRNA, wherein sample 1 contained 100 nM of *cel*-miR-54, sample 2 contained 100 nM of *hsa*-miR-21, and sample 3 contained 100 nM of *hsa*-miR-21 and 100 nM of *cel*-miR-39. Each sample was introduced into a different device, and the microRNA sensing assay was conducted based on a three-step process shown in Figure 5A including i. incubation of the sample to enable hybridization of the target miRNA to the ssDNA probe, ii. ligation of the universal biotinylated linker, and iii. labeling of the dye, streptavidin-r-phycoerythrin (SAPE). Wash steps were conducted between each step, and at the end of the assay, fluorescence microscopy was used to image the channel-embedded posts after the detection of miRNA expression in sample 1 (Figure 5C), sample 2 (Figure 5D), and sample 3 (Figure 5E). The bar plots with snapshots of the hydrogel posts show the expected dysregulation profiles for all three samples with negligible nonspecific fluorescence and a high signal-to-noise ratio. Additionally, by employing graphically encoded hydrogel posts, the platform enables the detection of multiple biomarkers or targets within a single device and using a single biological fluid sample, highlighting its potential to significantly reduce patient sample volumes as well as assay times. These results further demonstrate the feasibility of the proposed microfabrication approach for the

https://doi.org/10.1021/acsomega.4c05196
ACS Omega 2024, 9, 38096−38106

development of advanced and functional microfluidics-driven biosensing platforms.

CONCLUSION

This work presents a robust and highly versatile approach to microfluidic device fabrication that couples SLA 3D printing with hot embossing for rapid prototyping and cost-effective clean-room-free fabrication of functional PDMS-based microfluidic devices applicable to advanced biosensing applications. In addition to our strategy's accessibility and user-friendliness, a key aspect of this work is the demonstration of high fidelity between the digital design and final microfluidic device which can be attributed to i. the optimization of the 3D printing parameters, ii. the exceptional transfer accuracy of the metal mold-free hot embossing process (exceeding 94% and 98% in the vertical and lateral dimensions, respectively), and ii. the low surface roughness of the 3D-printed chips and PMMA molds, which promotes strong surface adhesion and facilitates robust plasma bonding.[44] The versatility and applicability of the fabrication approach were demonstrated by the successful preparation of three biomedical microfluidic devices applicable to advanced biosensing applications: a microsphere droplet generator, an SFL-based hydrogel microparticle synthesizer, and a microfluidic platform for multiplexed biosensing using channel-embedded hydrogel posts. Notably, the latter device was able to perform multiplexed miRNA detection and correctly elucidate the dysregulation pattern of three miRNAs within model biofluid sample solutions. This highlights the transformative potential of this approach in fabricating advanced lab-on-a-chip devices for biosensing and clinical diagnostic applications. By lowering the barriers to entry in microfluidic engineering - through eliminating the need for specialized personnel, expensive equipment, and cleanroom environments - the facile and novel approach introduced herein has the potential to revolutionize the field of biomicrofluidics and accelerate the translation of these powerful platforms from research laboratories to real-world problems.[45]

EXPERIMENTAL SECTION

Materials. Streptavidin, R-phycoerythrin (SAPE), and ATP were purchased from Thermo Fisher. All oligonucleotides used in this work including the ssDNA probes, universal biotinylated linker, and target miRNA were purchased from Integrated DNA Technologies (IDT), and their sequences can be found in the Supporting Information (Table S2). T4 DNA ligase and NEB2 buffer were purchased from New England Biolabs. Polyethylene glycol diacrylate (M_w = 700), 2-Hydroxy-2-methylpropiophenone (Darocur), sodium chloride (NaCl), and Tween-20 were purchased from Sigma-Aldrich. Polyethylene glycol (M_w = 600) was purchased from Acros Organics. 100xTris-EDTA (TE) buffer was purchased from EMD Millipore. Polydimethylsiloxane (Sylgard 184) was purchased from Dow Chemicals. Nuclease-free water was purchased from Omega Bio-Tek.

Methods. *Step 1. Fabrication of the 3D Printed Molds.* SOLIDWORKS 2022 software was used to design the desired mold structures, and the designs were subsequently exported in the form of standard triangle language files, which are compatible with the commercial Phrozen 3D printer (Phrozen Technology, Taiwan). The 3D printer contains a reservoir for the liquid resin, a UV LCD plate with 22-μm in xy and 10- μm resolution in z axis underneath the reservoir, and a building plate on top. Based on SLA, the system used a UV beam to expose the free surface of a liquid polymer, inducing photopolymerization and depositing of the solid structure onto the building plate. Excessive UV exposure would result in a slope on the channel walls, whereas insufficient exposure would result in the formation of isolated layers; therefore, exposure time was optimized to improve the channel and surface quality. Layer thickness should be quantized to the designed channel depth to achieve the highest precision; thus, a thickness of 42 μm was adopted herein. After printing, the molds were washed with acetone to remove the liquid residue and placed inside a UV box (Hoefer Inc., Massachusetts, US) for postcuring. The entire procedure was conducted at room temperature without the requirement for a cleanroom environment. TR300 Ultra-High Temp 3D Printing Resin was used as the printing material (Phrozen Technology, Taiwan).

Step 2. Hot Embossing onto PMMA. Based on the 3D print, a PMMA (Rowad Plastic Ltd., Saudi Arabia) replica was produced using a Sublym hot embossing machine (Eden Tech, Paris, France) as outlined in the following protocol. First, a 1 mm-thick acrylic chip was used to ensure its flexibility and deformation under pressure. The chip was cleaned with Kimwipes (KIMTECH), followed by blowing with nitrogen gas to remove any dust particles on the surface. Prior to hot embossing, the acrylic chip was placed at the bottom of the embossing chamber, adjacent to the heating plate, above which the 3D printed design was placed, followed by a piece of quartz of the same size as the chip. Hot embossing was conducted at a pressure of 400 MPa and a temperature of 165°C, which exceeds the glass transition temperature of PMMA. Heating was stopped after 15 min but the high pressure was maintained until the temperature reached 90°C to ensure successful feature replication onto the acrylic chip. This demolding temperature was chosen as it facilitated the separation of the acrylic chip from the 3D-printed design while maintaining high surface quality.[46]

Steps 3 and 4. Microfluidic device fabrication: PDMS Casting and Plasma Bonding. After mold preparation, a PDMS-on-glass microfluidic device was prepared, as outlined herein. Briefly, as the PMMA molds were designed to have inlets and outlets, holes and side walls were made using a carbon dioxide (CO_2) laser. Further, plastic tubes were inserted to create inlet and outlet channels. This technique omits the need for punching holes through PDMS, ensuring consistency and further simplifying the fabrication approach. Next, PDMS at a 10:1 (w/w) base-to-curing agent ratio was cast onto the PMMA mold and cured at 60 °C for 2 h. For the biomedical microfluidic devices, the final devices were assembled and sealed by plasma bonding the PDMS on a glass coverslip (oxygen plasma treatment, 40 s), followed by heating to 80°C for 15 min to anneal and strengthen the bonding. For the SFL-based hydrogel microparticle synthesizer device, prior to bonding, a thin layer of PDMS was spin-coated onto the glass surface. Due to its excellent oxygen permeability, this PDMS layer inhibits polymerization at the channel surfaces (through oxygen inhibition of radical polymerization) to prevent particles from sticking onto the channel.[39]

Characterization of the Microchannel Dimensions and Surface Roughness. The designed microfluidic channels comprised a hydrodynamic flow-focusing structure, as shown in Figure 1A, highlighting a small nozzle with a narrow channel

https://doi.org/10.1021/acsomega.4c05196
ACS Omega 2024, 9, 38096−38106

designed to promote the squeezing effect of the central flow. The microfluidic device was designed to have a depth, main channel width, and nozzle width of 126 μm, 300 μm, and 154 μm, respectively. The microchannel profile and surface morphology of the 3D prints and PMMA replicas were measured by the DektakXT (Bruker, Massachusetts, US) stylus profilometer. The stylus scanned across the channel and surface within 30 s and conducted height measurements at 9000 points. It is noteworthy that the reported measurements are affected by profilometer tip size and thus the real measurements are likely better than reported. A random point was chosen for each chip, and three chips were analyzed to provide an estimate of the average accuracy. The collected data was plotted on Origin software to compare with the design.

Preparation of Three Microfluidics-driven Biosensing Platforms. To demonstrate the versatility of our facile microfabrication approach, three types of biomicrofluidic devices were fabricated: a microsphere droplet generation, an SFL-based hydrogel microparticle fabrication, and a hydrogel postembedded microfluidic device for multiplexed biomarker detection. For the droplet generator, sunflower oil was adopted as the continuous phase while distilled water was used as the dispersed phase. Standard PHD ULTRA syringe pumps (Harvard Apparatus, Massachusetts, US) were used for fluidic control. The focusing region was observed using a 10x objective lens on an upright brightfield microscope (Axio Examiner D1, Zeiss, US). Microsphere droplet generation was recorded using a high-speed camera (Chronos 2.1, Kron Technologies, Canada), and the droplet dimensions were analyzed using ImageJ software and Matlab, and plotted using Graphpad Prism.

For the SFL-based hydrogel microparticle fabrication, the experimental configuration was based on a previously reported study,[39] with the devices being fabricated using the proposed methodology developed herein. Briefly, a compressed air pressure source with an electrically powered valve was used to control the fluid (hydrogel precursor) flow inside the microfluidic channel. A shutter was also employed within an inverted fluorescence microscope to control the UV light exposure from a UV LED (Thorlabs M365L2) through a defined photomask for photopolymerization. An Arduino microprocessor was programmed to simultaneously control the fluidic valve and microscope shutter to enable the high-throughput fabrication of hydrogel microparticles within the microfluidic channels. The hydrogel precursor solution, which was based on previous work and optimized for biosensing assays,[47] consisted of 20% polyethylene glycol diacrylate 700 (PEGDA700), 40% polyethylene glycol 600 (PEG600), 35% 3xTris-EDTA (3xTE) buffer, and 5% Darocur as a photo-initiator.

A similar setup was adopted for the third application consisting of a hydrogel postembedded microfluidic channel; however, in this device assembly, the glass coverslip was not coated with a PDMS layer which enabled immobilization of the hydrogel posts within the channel. Three model samples with different expression levels of miRNA were prepared. Sample 1 denoted as 001 contained 100 nM of *cel*-miR-54, sample 2 denoted as 010 contained 100 nM of *hsa*-miR-21, while sample 3 denoted as 011 contained 100 nM of *hsa*-miR-21 and 100 nM of *cel*-miR-39, prepared in hybridization buffer containing 1× Tris-EDTA buffer with 0.05% Tween-20 (1× TET) and 500 mM NaCl. Next, the solutions were introduced to the channel and incubated at 55 °C for 90 min. For linker ligation, 250 μL of ligation solution containing 10% (v/v) 10× NEB2 buffer, 2.5% (v/v) ATP, 0.4% (v/v) 10 μM biotinylated linker, 0.2% (v/v) T4 DNA ligase in TET buffer was introduced to the channel.[40] The ligation reaction was conducted at 21.5 °C for 1 h. Finally, fluorescence labeling was conducted with 10 μg/mL of streptavidin-*r*-phycoerythrin (SAPE) at 21.5 °C for 1 h. All steps were conducted on a thermoshaker under 250 rpm agitation, followed by four washing steps with 250 μL of rinse buffer (1× TET with 50 mM NaCl) in between each step. After the biosensing assays were conducted, the microfluidic chips were placed under an inverted fluorescence microscope (Zeiss Axio Observer) equipped with an LED excitation source (X-Cite 120 LED) and a filter (Semrock ex = 520/60, em = 607/70) for imaging using a 20× objective lens. Images were analyzed using Imagej software.

■ ASSOCIATED CONTENT

Supporting Information

The Supporting Information is available free of charge at https://pubs.acs.org/doi/10.1021/acsomega.4c05196.

Literature review table and a table of the oligonucleotide sequences used in this work (PDF)

■ AUTHOR INFORMATION

Corresponding Author

Dana Alsulaiman − *Division of Physical Science & Engineering, King Abdullah University of Science and Technology (KAUST), Thuwal, Makkah Province 23955-6900, Kingdom of Saudi Arabia;* orcid.org/0000-0002-3185-6288; Email: dana.alsulaiman@kaust.edu.sa

Authors

Haoliang Lu − *Division of Physical Science & Engineering, King Abdullah University of Science and Technology (KAUST), Thuwal, Makkah Province 23955-6900, Kingdom of Saudi Arabia*

Almas Rakhymzhanov − *Nanofabrication Core Lab, King Abdullah University of Science and Technology (KAUST), Thuwal, Makkah Province 23955-6900, Kingdom of Saudi Arabia*

Ulrich Buttner − *Nanofabrication Core Lab, King Abdullah University of Science and Technology (KAUST), Thuwal, Makkah Province 23955-6900, Kingdom of Saudi Arabia*

Complete contact information is available at: https://pubs.acs.org/10.1021/acsomega.4c05196

Notes

The authors declare no competing financial interest.

■ ACKNOWLEDGMENTS

The authors acknowledge King Abdullah University of Science and Technology (KAUST) for funding this research.

■ REFERENCES

(1) Krauss, S. T.; Woolf, M. S.; Hadley, K. C.; Collins, N. M.; Nauman, A. Q.; Landers, J. P. Centrifugal Microfluidic Devices Using Low-Volume Reagent Storage and Inward Fluid Displacement for Presumptive Drug Detection. *Sens. Actuators, B* **2019**, *284*, 704−710.
(2) Ramanathan, N.; Simakov, O.; Merten, C. A.; Arendt, D. Quantifying Preferences and Responsiveness of Marine Zooplankton

to Changing Environmental Conditions Using Microfluidics. *PLoS One* **2015**, *10* (10), e0140553.
(3) Bringer, M. R.; Gerdts, C. J.; Song, H.; Tice, J. D.; Ismagilov, R. F. Microfluidic Systems for Chemical Kinetics That Rely on Chaotic Mixing in Droplets. *Philos. Trans. R. Soc. A Math. Phys. Eng. Sci.* **2004**, *362* (1818), 1087−1104.
(4) Cook, S. R.; Musgrove, H. B.; Throckmorton, A. L.; Pompano, R. R. Microscale Impeller Pump for Recirculating Flow in Organs-on-Chip and Microreactors. *Lab Chip* **2022**, *22* (3), 605−620.
(5) Gowers, S. A. N.; Curto, V. F.; Seneci, C. A.; Wang, C.; Anastasova, S.; Vadgama, P.; Yang, G. Z.; Boutelle, M. G. 3D Printed Microfluidic Device with Integrated Biosensors for Online Analysis of Subcutaneous Human Microdialysate. *Anal. Chem.* **2015**, *87* (15), 7763−7770.
(6) Eduati, F.; Utharala, R.; Madhavan, D.; Neumann, U. P.; Longerich, T.; Cramer, T.; Saez-Rodriguez, J.; Merten, C. A. A Microfluidics Platform for Combinatorial Drug Screening on Cancer Biopsies. *Nat. Commun.* **2018**, *9* (1), No. 2434, DOI: 10.1038/s41467-018-04919-w.
(7) Yeong, W. Y.; Sudarmadji, N.; Yu, H. Y.; Chua, C. K.; Leong, K. F.; Venkatraman, S. S.; Boey, Y. C. F.; Tan, L. P. Porous Polycaprolactone Scaffold for Cardiac Tissue Engineering Fabricated by Selective Laser Sintering. *Acta Biomater.* **2010**, *6* (6), 2028−2034.
(8) Sibbitt, J. P.; He, M. 3D PRINTING OF MICROFLUIDICS FOR POINT OF CARE DIAGNOSIS. *Proc. ASME Int. Manuf. Sci. Eng. Conf.* **2017**, V004T05A002.
(9) Kulkarni, M. B.; Ayachit, N. H.; Aminabhavi, T. M.; Pogue, B. W. Recent Advances in Microfluidics-Based Paper Analytical Devices (MPADs) for Biochemical Sensors: From Fabrication to Detection Techniques. *Biochem. Eng. J.* **2023**, *198* (June), No. 109027.
(10) Kulkarni, M. B.; Ayachit, N. H.; Aminabhavi, T. M. A Short Review on Miniaturized Biosensors for the Detection of Nucleic Acid Biomarkers. *Biosensors* **2023**, *13* (3), 412.
(11) Kulkarni, M. B.; Ayachit, N. H.; Aminabhavi, T. M. Recent Advances in Microfluidics-Based Electrochemical Sensors for Foodborne Pathogen Detection. *Biosensors* **2023**, *13* (2), 246.
(12) Kulkarni, M. B.; Ayachit, N. H.; Aminabhavi, T. M. Recent Advancements in Nanobiosensors: Current Trends, Challenges, Applications, and Future Scope. *Biosensors* **2022**, *12* (10), 892.
(13) Kulkarni, M. B.; Ayachit, N. H.; Aminabhavi, T. M. Biosensors and Microfluidic Biosensors: From Fabrication to Application. *Biosensors* **2022**, *12* (7), 543.
(14) Whitesides, G. M.; Ostuni, E.; Takayama, S.; Jiang, X.; Ingber, D. E. Soft Lithography in Biology. *Annu. Rev. Biomed. Eng.* **2001**, *3*, 335−373.
(15) Sanchez Noriega, J. L.; Chartrand, N. A.; Valdoz, J. C.; Cribbs, C. G.; Jacobs, D. A.; Poulson, D.; Viglione, M. S.; Woolley, A. T.; Van Ry, P. M.; Christensen, K. A.; Nordin, G. P. Spatially and Optically Tailored 3D Printing for Highly Miniaturized and Integrated Microfluidics. *Nat. Commun.* **2021**, *12* (1), No. 5509, DOI: 10.1038/s41467-021-25788-w.
(16) Jin, Y.; Xiong, P.; Xu, T.; Wang, J. Time-Efficient Fabrication Method for 3D-Printed Microfluidic Devices. *Sci. Rep.* **2022**, *12* (1), 1−9.
(17) Najmon, J. C.; Raeisi, S.; Tovar, A. Review of Additive Manufacturing Technologies and Applications in the Aerospace Industry. In *Additive Manufacturing for the Aerospace Industry*; Froes, F., Boyer, R., Eds.; Elsevier Inc., 2019; pp 7−13.
(18) Schmidleithner, C.; Kalaskar, D. M. Stereolithography. In *2D Printing*; Cvetković, D., Ed.; Intech, 2016. DOI: 10.5772/intechopen.78147.
(19) Felton, H.; Hughes, R.; Diaz-Gaxiola, A. Negligible-Cost Microfluidic Device Fabrication Using 3D-Printed Interconnecting Channel Scaffolds. *PLoS One* **2021**, *16*, e0245206.
(20) Razavi Bazaz, S.; Kashaninejad, N.; Azadi, S.; Patel, K.; Asadnia, M.; Jin, D.; Ebrahimi Warkiani, M. Rapid Softlithography Using 3D-Printed Molds. *Adv. Mater. Technol.* **2019**, *4* (10), No. 1900425, DOI: 10.1002/admt.201900425.
(21) Pham, P. H.; Dao, D. V.; Amaya, S.; Kitada, R.; Sugiyama, S. Fabrication and Characterization of Smooth Si Mold for Hot Embossing Process. *IEEJ. Trans. Sensors Micromachines* **2007**, *127* (3), 187.
(22) Lin, T. Y.; Do, T.; Kwon, P.; Lillehoj, P. B. 3D Printed Metal Molds for Hot Embossing Plastic Microfluidic Devices. *Lab Chip* **2017**, *17* (2), 241−247.
(23) Deshmukh, S. S.; Goswami, A. Hot Embossing of Polymers - A Review. *Mater. Today Proc.* **2020**, *26*, 405−414.
(24) Fouassier, J. P.; Allonas, X.; Lalevée, J.; Dietlin, C. Photoinitiators for Free Radical Polymerization Reactions. In *Photochemistry and Photophysics of Polymeric Materials*; Allen, N. S., Ed.; Wiley, 2010.
(25) Dzadz, Ł.; Pszczółkowski, B. Analysis of the Influence of UV Light Exposure Time on Hardness and Density Properties of SLA Models. *Technol. Sci.* **2000**, No. 2020.
(26) Miedzińska, D.; Gieleta, R.; Popławski, A. Experimental Study on Influence of Curing Time on Strength Behavior of Sla-Printed Samples Loaded with Different Strain Rates. *Materials* **2020**, *13* (24), 5825.
(27) Debenedetti, P. G.; Stillinger, F. H. Supercooled Liquids and the Glass Transition. *Nature* **2001**, *410* (March), 259.
(28) Wang, Y.; Hansen, C. J.; Wu, C. C.; Robinette, E. J.; Peterson, A. M. Effect of Surface Wettability on the Interfacial Adhesion of a Thermosetting Elastomer on Glass. *RSC Adv.* **2021**, *11* (49), 31142−31151.
(29) Saxena, S.; Joshi, R. Microfluidic Devices: Applications and Role of Surface Wettability in Its Fabrication. *21st Century Surf. Sci. - a Handb.* **2020**, 1−19.
(30) Shun'ko, E. V.; Belkin, V. S. Cleaning Properties of Atomic Oxygen Excited to Metastable State $2s^2 2p^4$ (^{1}S1). *J. Appl. Phys.* **2007**, *102* (8), No. 083304, DOI: 10.1063/1.2794857.
(31) Bhattacharya, S.; Datta, A.; Berg, J. M.; Gangopadhyay, S. Studies on Surface Wettability of Poly(Dimethyl) Siloxane (PDMS) and Glass under Oxygen-Plasma Treatment and Correlation with Bond Strength. *J. Microelectromechanical Syst.* **2005**, *14* (3), 590−597.
(32) Balbino, T. A.; Serafin, J. M.; Radaic, A.; de Jesus, M. B.; de la Torre, L. G. Integrated Microfluidic Devices for the Synthesis of Nanoscale Liposomes and Lipoplexes. *Colloids Surfaces B Biointerfaces* **2017**, *152*, 406−413.
(33) Liu, L.; Xu, K.; Wang, H.; Jeremy Tan, P. K.; Fan, W.; Venkatraman, S. S.; Li, L.; Yang, Y. Y. Self-Assembled Cationic Peptide Nanoparticles as an Efficient Antimicrobial Agent. *Nat. Nanotechnol.* **2009**, *4* (7), 457−463.
(34) Gkionis, L.; Campbell, R. A.; Aojula, H.; Harris, L. K.; Tirella, A. Manufacturing Drug Co-Loaded Liposomal Formulations Targeting Breast Cancer: Influence of Preparative Method on Liposomes Characteristics and in Vitro Toxicity. *Int. J. Pharm.* **2020**, *590* (July), No. 119926.
(35) Pinheiro, L. B.; Coleman, V. A.; Hindson, C. M.; Herrmann, J.; Hindson, B. J.; Bhat, S.; Emslie, K. R. Evaluation of a Droplet Digital Polymerase Chain Reaction Format for DNA Copy Number Quantification. *Anal. Chem.* **2012**, *84* (2), 1003−1011.
(36) Zhao, S.; Lin, H.; Chen, S.; Yang, M.; Yan, Q.; Wen, C.; Hao, Z.; Yan, Y.; Sun, Y.; Hu, J.; Chen, Z.; Xi, L. Sensitive Detection of Porcine Circovirus-2 by Droplet Digital Polymerase Chain Reaction. *J. Vet. Diagnostic Investig.* **2015**, *27* (6), 784−788.
(37) Brunetto, G. S.; Massoud, R.; Leibovitch, E. C.; Caruso, B.; Johnson, K.; Ohayon, J.; Fenton, K.; Cortese, I.; Jacobson, S. Digital Droplet PCR (DdPCR) for the Precise Quantification of Human T-Lymphotropic Virus 1 Proviral Loads in Peripheral Blood and Cerebrospinal Fluid of HAM/TSP Patients and Identification of Viral Mutations. *J. Neurovirol.* **2014**, *20* (4), 341−351.
(38) Zhao, H.; Wilkins, K.; Damon, I. K.; Li, Y. Specific QPCR Assays for the Detection of Orf Virus, Pseudocowpox Virus and Bovine Papular Stomatitis Virus. *J. Virol. Methods* **2013**, *194* (1−2), 229−234.

https://doi.org/10.1021/acsomega.4c05196
ACS Omega 2024, 9, 38096−38106

(39) Dendukuri, D.; Gu, S. S.; Pregibon, D. C.; Hatton, T. A.; Doyle, P. S. Stop-Flow Lithography in a Microfluidic Device. *Lab Chip* **2007**, 7 (7), 818−828.
(40) Al Sulaiman, D.; Juthani, N.; Doyle, P. S. Quantitative and Multiplex Detection of Extracellular Vesicle-Derived. *Adv. Healthc. Mater.* **2022**, *11*, No. 2102332.
(41) Al Sulaiman, D.; Shapiro, S. J.; Gomez-Marquez, J.; Doyle, P. S. High-Resolution Patterning of Hydrogel Sensing Motifs within Fibrous Substrates for Sensitive and Multiplexed Detection of Biomarkers. *ACS Sensors* **2021**, *6* (1), 203−211.
(42) Bartel, D. P. MicroRNAs: Genomics, Biogenesis, Mechanism, and Function. *Cell* **2004**, *116* (2), 281−297.
(43) Wu, L.; Wang, Y.; He, R.; Zhang, Y.; He, Y.; Wang, C.; Lu, Z.; Liu, Y.; Ju, H. Fluorescence Hydrogel Array Based on Interfacial Cation Exchange Amplification for Highly Sensitive MicroRNA Detection. *Anal. Chim. Acta* **2019**, *1080*, 206−214.
(44) Kang, K.; Yoo, K.-P.; Paek, S.-H.; Min, N.-K. Surface Roughness Effect for PDMS Direct Bonding. *ECS Meet. Abstr.* **2006**, *MA2005-02* (11), No. 436.
(45) Tang, S. K. Y.; Whitesides, G. M. Basic Microfluidic and Soft Lithographic Techniques. In *Optofluidics: Fundamentals, Devices and Applications*; Fainman, Y., Lee, L. P., Psaltis, D., Yang, C., Eds.; McGraw-Hill, 2010; pp 7−32.
(46) Dirckx, M. E.; Hardt, D. E. Analysis and Characterization of Demolding of Hot Embossed Polymer Microstructures. *J. Micromechanics Microengineering* **2011**, *21* (8), 085024.
(47) Choi, N. W.; Kim, J.; Chapin, S. C.; Duong, T.; Donohue, E.; Pandey, P.; Broom, W.; Hill, W. A.; Doyle, P. S. Multiplexed Detection of MRNA Using Porosity-Tuned Hydrogel Microparticles. *Anal. Chem.* **2012**, *84* (21), 9370−9378.

https://doi.org/10.1021/acsomega.4c05196
ACS Omega 2024, 9, 38096−38106